POLITECNICO DI TORINO
Repository ISTITUZIONALE

Creation of pure non-crystalline diamond nanostructures via room-temperature ion irradiation and subsequent thermal annealing

(Article begins on next page)

19 April 2024

Nanoscale
Advances

Accepted Manuscript

Volume 1
Number 1
January 2018
Pages 1-200

Nanoscale
Advances

rsc.li/nanoscale-advances

ISSN 2516-0230

ROYAL SOCIETY
OF CHEMISTRY

NCNST

ROYAL SOCIETY
OF CHEMISTRY

rsc.li/nanoscale-advances

1 **Creation of pure non-crystalline diamond nanostructures via**

2 **room-temperature ion irradiation and subsequent thermal annealing**

3

4 F. Picollo[1,2], A. Battiato[2], F. Bosia[1,3], F. Scaffidi Muta[1],

5 P. Olivero[1,2]*, V. Rigato[4], S. Rubanov[5]

6

7 [1]Physics Department and "NIS inter-departmental centre", University of Torino, Torino 10125, Italy

8 [2]National Institute of Nuclear Physics, Section of Torino, Torino 10125, Italy

9 [3]Applied Science and Technology Department, Politecnico di Torino, Torino 10129, Italy

10 [4]National Institute of Nuclear Physics, National Laboratories of Legnaro, Legnaro 35020, Italy

11 [5]Bio21 Institute, the University of Melbourne, Victoria 3010, Australia

12

13 * corresponding author: paolo.olivero@unito.it

14

15 Carbon exhibits a remarkable range of structural forms, due to the availability of sp^3, sp^2 and

16 sp^1 chemical bonds. Contrarily to other group IV elements such as silicon and germanium,

17 the formation of an amorphous phase based exclusively on sp^3 bonds is extremely

18 challenging due to the strongly favored formation of graphitic-like structures at room

19 temperature and pressure. As such, the formation of a fully sp^3-bonded carbon phase requires

20 an extremely careful (and largely unexplored) definition of the pressure and temperature

21 across the phase diagram. Here, we report on the possibility of creating full-sp^3 amorphous

22 nanostructures within the bulk crystal of diamond with room-temperature ion-beam

23 irradiation, followed by an annealing process that does not involve the application of any

24 external mechanical pressure. As confirmed by numerical simulations, the (previously

25 unreported) radiation-damage-induced formation of an amorphous sp^2-free phase in diamond

26 is determined by the buildup of extremely high internal stresses from the surrounding lattice,

27 which (in the case of nanometer-scale regions) fully prevent the graphitization process.

28 Besides the relevance of understanding the formation of exotic carbon phases, the use of

29 focused/collimated ion beams discloses appealing perspectives for the direct fabrication of

30 such nanostructures in complex three-dimensional geometries.

1. Introduction

31

32 Carbon is an extremely "versatile" chemical element due to the availability of different types

33 of hybridized chemical bonds (sp^1, sp^2 and sp^3), that determine a remarkable range of

34 possible allotropic forms, both in bulk form and as nanostructures [1]. In many respects,

35 diamond lies at the very extreme of such a range, as far as bulk structures are concerned: due

36 to is strong covalent sp^3 bond, the diamond crystal is characterized by extreme mechanical

37 (high hardness, low friction coefficient), optical (broad transparency from the near UV to the

38 far IR), thermal (large thermal conductivity, low thermal expansion coefficient) and electrical

39 (extreme dielectric strength, high carrier mobility) properties [2]. These unique characteristics

40 have motivated a remarkable body of scientific work aimed at better understanding its

41 fundamental properties, as well as its synthesis and application in many different

42 technological fields, ranging from high-power to quantum devices, encompassing biosensors,

43 MEMS technology and much more [3-5]. Not only has the systematic production of

44 high-quality artificial diamond crystals via high-pressure-high-temperature (HPHT) [6] and

45 chemical-vapor-deposition (CVD) [7] techniques made remarkable progress in the past

46 decades, but the development of devices based on micro- and nano-crystalline diamond has

47 also attracted ever-increasing interest, thanks to the fact that several appealing characteristics

48 (most remarkably mechanical ones) are largely preserved in a material platform requiring less

49 sophisticated synthesis methods [8].

50 Moving towards more "defective" and technologically viable forms of sp^3-bonded carbon,

51 different forms of polycrystalline diamond [9], ultra-nanocrystalline diamond [10],

52 nano-twinned diamond [11] and amorphous diamond-like carbon [12, 13] have been widely

53 investigated for several decades, with the promise of further expanding the applicability of

54 extreme physical properties into technological landscapes in which synthesis and fabrication

55 techniques can be realistically scaled to large production volumes. In this context, the higher

56 thermodynamical stability of sp^2-bonded carbon at room pressure and temperature conditions

57 represents a fundamental limitation: in these conditions, graphite and graphite-like phases

58 constitute the ultimate "ground state" for carbon structures when a critical amount of

59 structural disorder is introduced. For this reason, substantial efforts have been made in the

60 synthesis of amorphous carbon phases characterized by a high fraction of sp^3 bonds [14-16],

61 but the pursuit of a 100% fully sp^3-bond amorphous carbon phase is still ongoing. A careful

62 control of environmental parameters (pressure in particular) allows the engineering of novel

63 forms of carbon, as demonstrated by the fact that exerting high (i.e. $\sim 10^2$ GPa) pressures on

64   glassy carbon (i.e. an amorphous sp^2 phase) yields the formation of phases characterized by

65   high sp^3 content with no long-range ordering, whose structural stability can to some extent be

66   tuned if an equally careful control of temperature variable can be achieved [17-19]. In this

67   context, a powerful and versatile tool is represented by the local laser heating of different

68   types of carbon structures under different mechanical stress conditions, either exerted from

69   external pressure sources [20] or established within the sample by the coexistence of carbon

70   phases characterized by different densities and mechanical properties [21].

71   Local laser heating was combined with the possibility offered by MeV ion irradiation to

72   create sub-superficial graphitic structures within bulk diamond thanks to the strongly

73   non-linear damage profile of energetic ions in matter. The ion-damage-induced collapse into

74   a graphitic phase of layers with sub-μm thickness localized within the diamond crystal

75   determines substantial local variations in both atomic density and mechanical parameters

76   (Young's and shear moduli), that can in turn develop strong (i.e. ~10 GPa) and highly

77   localized internal stresses, without the need of using external pressure sources [22]. In these

78   conditions, optical absorption of the laser light at different power densities from the

79   sub-superficial compressed graphitic layers allowed a fine control of local temperature

80   variations, and thus an accurate exploration of the graphite-diamond-liquid triple point [23].

81   In this context, the employment of other types of radiation (e.g. x-ray nano-beams) could be

82   successfully employed to engineer structural damage with high spatial resolution, as already

83   successfully demonstrated in other types of substrates [24-26].

84   More recently, a careful control of the *in situ* laser-induced heating of glassy carbon kept at

85   high (i.e. ~50 GPa) pressure by means of a diamond anvil cell allowed the exploration of a

86   very specific (and up to then scarcely studied) portion of the phase diagram of carbon, which

87   resulted in the first demonstration of the synthesis of quenchable fully-sp^3 bonded amorphous

88   carbon phase. This stable amorphous phase of carbon was unequivocally demonstrated to be

89   based on a sp^2-free structure by means of high-resolution transmission electron microscopy

90   (HRTEM) and electron energy loss spectroscopy (EELS), and exhibited properties of optical

91   transparency, high density and extreme stiffness that were comparable to those of diamond

92   [20].

93   In the present work, we take advantage of a high-resolution lithographic technique based on

94   the use of masked MeV ions to define sub-superficial amorphous nanostructures in the

95   diamond bulk induced by atomic collisions. We demonstrate by means of HRTEM and EELS

96   that these structures are lacking any measurable fraction of sp^2 bonds, specifically because

97 their size (i.e. ~100-200 nm, depending upon fabrication parameters) and depth below the

98 crystal surface (i.e. ~1.6 µm) is such to inhibit any form of graphitization by the development

99 of strong (i.e. >40 GPa) internal pressures. These results demonstrate for the first time the

100 possibility of direct MeV-ion-beam writing with high spatial resolution a quenchable

101 amorphous phase in diamond at room conditions, with no need of externally applied

102 pressures.

103

104 **2. Results and discussion**

105 Radiation-hard contact masks were lithographically defined at high spatial resolution on

106 single-crystal diamond samples, with the purpose of allowing ion irradiation across

107 nanometer-sized regions. To achieve this, focused ion beam (FIB) micromachining was

108 performed on a ~1.3 µm thick Copper layer deposited on the sample surface, resulting in the

109 formation of linearly shaped nano-apertures with 100 nm lateral width, as schematically

110 shown in Fig. 1. Notice that across the FIB-micromachined apertures the sample surface was

111 not fully exposed, but rather a ~100 nm thick metal layer was left at the bottom of the

112 aperture to avoid the contamination of the diamond surface with the milling Ga^+ ion beam.

113 After mask preparation, the samples were irradiated with a 1 MeV He^+ ion beam at

114 5×10^{16} cm^{-2} fluence. As schematically shown in the inset plot of Fig. 1, the energy and

115 fluence of implanted ions was such that across the exposed areas a sub-superficial highly-

116 damaged layer was formed in correspondence of the end-of-range "Bragg peak" of the ion

117 damage profile, i.e. ~1.6 µm. Conversely, the irradiation occurring just below the masked

118 regions resulted in the formation of a shallow (i.e. ~500 nm) damaged region. Overall, as

119 schematically shown in Fig. 1a (and experimentally highlighted in Fig. 4a), ion-induced

120 structural damage resulted in the formation of sub-superficial narrow regions (referred to as

121 "nanochannels" in the following) located below an extended shallow region (referred as

122 "continuous shallow layer" in the following). The ~500 nm thick layer of diamond comprised

123 between the continuous shallow layer and the sample surface will be referred as "cap layer"

124 in the following. The mask thickness was specifically chosen to allow the formation of the

125 continuous shallow layer, that acted as the "reference" damaged region with respect to the

126 nanochannels. The main difference between these two types of structures consists in the

127 depth at which they are formed, since they are created upon the same irradiation carried over

128 the very same time.

129   After MeV ion irradiation and subsequent mask removal, the samples were thermally
130   annealed in vacuum at 950 °C, with the scope of allowing the structural reorganization of the
131   highly damaged buried nano-regions, while removing residual damage from the regions
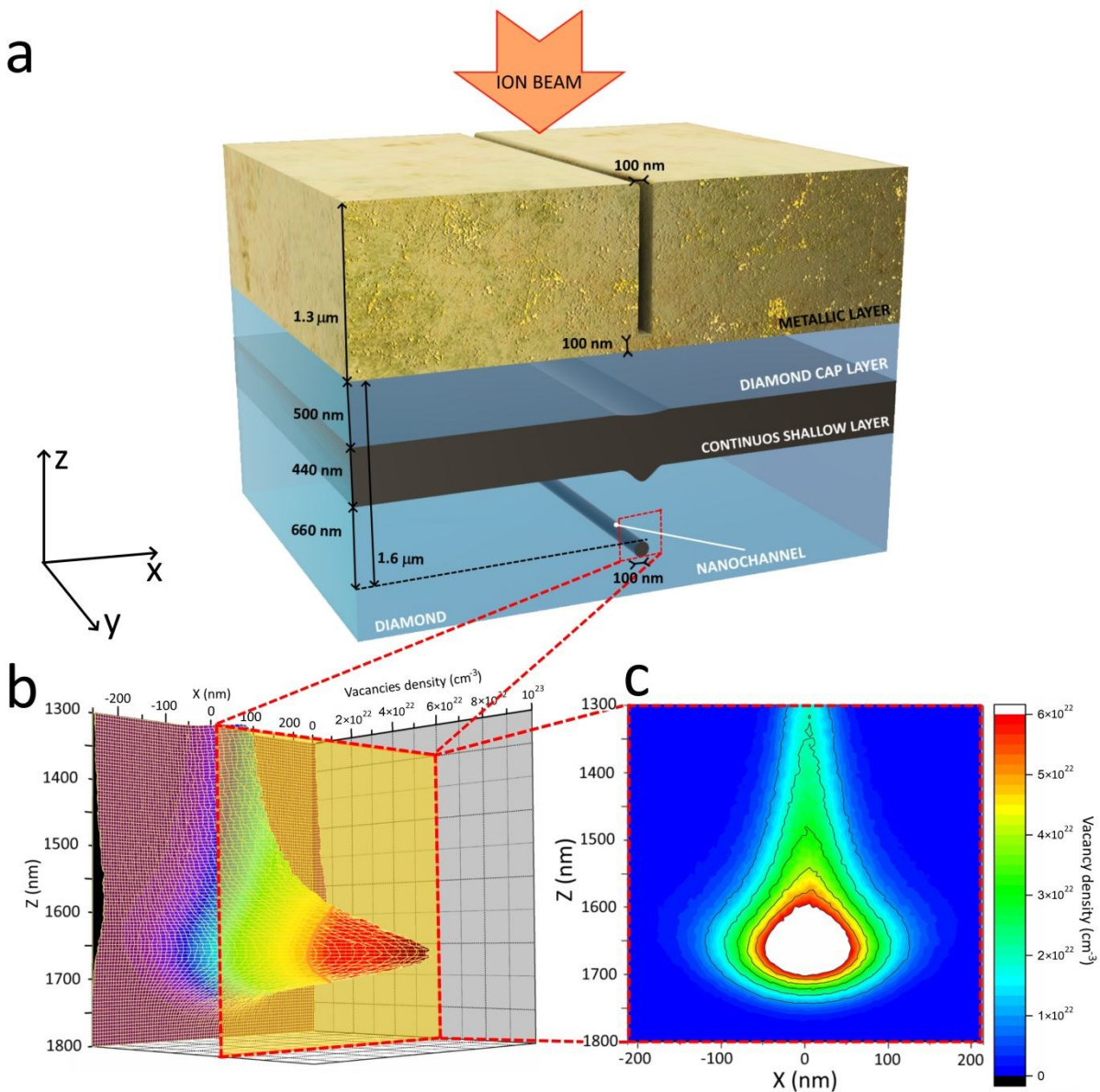132   irradiated at intermediate depths.

133

Fig. 1 *Sample geometry and profile of the ion-induced structural damage.* *a* *Schematic representation of the*
sample geometry: the metallic mask with the nanometric aperture determines the formation of both the
continuous shallow layer and of the nanochannel upon MeV ion irradiation. *b* *Three-dimensional plot of the*
cross-sectional profile of ion-induced damage density as resulting from SRIM simulation. *c* *Corresponding*
two-dimensional plot: the size and shape of the region damaged beyond the estimated critical threshold (in red)
corresponds to the features observed in Fig. 4a; note that the same plot is reported as an inset of Fig. 4a for
sake of comparison with experimental data.

141

142 The nanochannels of highly-damaged carbon phase are expected to form where the structural

143 damage (here parameterized as a volume density of created vacancies, as predicted by the

144 SRIM Monte Carlo simulation code [27] in a linear approximation) exceeds a critical

145 threshold, whose value has been estimated as $\sim(6.4 \pm 1.5)\times10^{22}$ cm^{-3} on the basis of the

146 measured dimensions of the nanostructures (see Figs. 1b-c and Fig. 4a).

147 This value is in good agreement with previous estimations of the parameter, commonly

148 referred to as "graphitization threshold", in the $(5–7)\times10^{22}$ cm^{-3} range [28-32]. As shown in

149 Fig. 1 (as well as in the inset of Fig. 4a), the SRIM-based model of the damage profile (which

150 also suitably describes the trajectories of laterally straggled ions) accurately predicts not only

151 the ~1.6 µm depth of the nanochannels below the surface, but also their overall shape.

152 As shown in Figs. 2a and 2b, the bright-field TEM cross-sectional micrograph and related

153 selected area diffraction pattern indicate that the as-irradiated microstructures consist of a

154 fully amorphized phase. Remarkably, the same is observed also after the annealing step (see

155 Figs. 2c and 2d), thus indicating that the thermal process stabilizes the structures without

156 inducing any re-crystallization of either sp^2 or sp^3 phases. Dark contours are also visible

157 around the nanostructures, indicating lattice strains due to a high local concentration of point

158 defects. The diffraction patterns in Figs. 2b and 2d only show broad rings that are typical of

159 amorphous structures. It is worth remarking that the radius of the first ring correlates with the

160 positions of the {111} diffraction spots generated from the surrounding crystalline diamond

161 matrix, as reported in the reference diffraction pattern reported in the inset of Fig. 2. This

162 confirms that the probed phase is fully amorphized. The absence in the diffraction patterns of

163 features related to sp^2 bonding (i.e. rings corresponding to the {002} lattice plane of graphite)

164 can be attributed to a low fraction of sp^2 bonds or to a predominant orientation of graphite

165 basal plains normal to the electron beam direction.

166 In order to provide direct insight into the nature of the chemical bonds within the amorphized

167 nano-regions, EELS analysis was carried both before and after thermal annealing, in the

168 energy ranges corresponding to the K absorption edge of carbon and the plasmonic energy

169 loss. As far as the former energy range is concerned (see Fig. 3a), the K-edge EELS spectra

170 acquired from the nanostructure before thermal annealing are entirely lacking the articulated

171 post-edge structures observed in the corresponding spectra acquired from the surrounding

172 diamond matrix. Remarkably, this clear distinction in EELS spectral features is fully

173 preserved after the annealing step, thus indicating that no phases attributable to crystalline

174 diamond can be detected upon thermal processing.

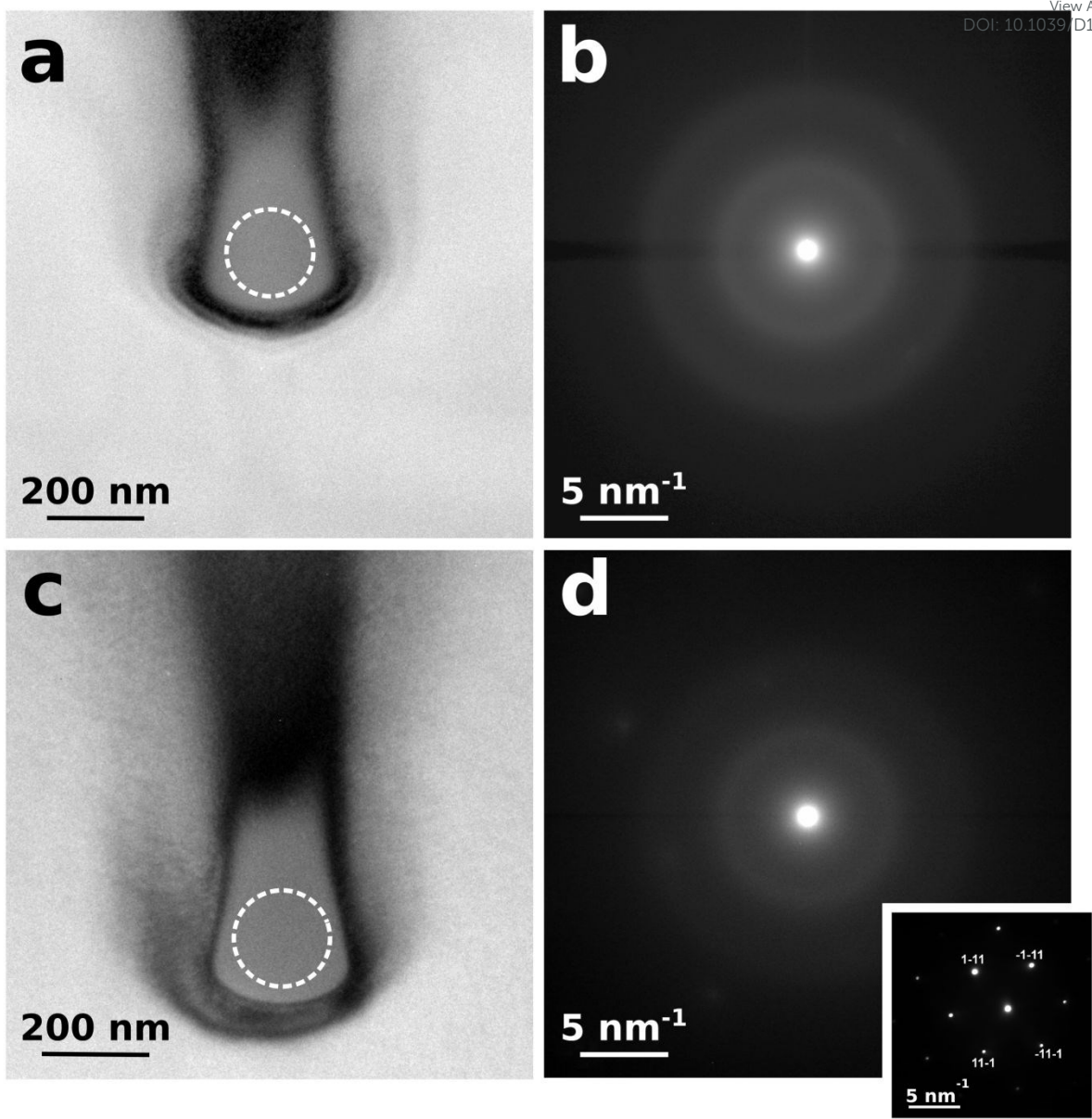"Direct Creation of Amorphous Diamond Nanostructures via Ion Irradiation"   p. 7

Fig. 2 Results of cross-sectional TEM characterization of a nanostructure. *a* Bright-field TEM micrograph from the as-implanted structure and *b* corresponding diffraction pattern collected from the area highlighted by the dashed circle in a. *c* Bright-field TEM micrograph from the same structure after thermal annealing and *d* corresponding diffraction pattern collected from the area highlighted by the dashed circle in c. A diffraction pattern from the surrounding diamond matrix is reported in the inset for reference purpose.

Note that the spectra acquired from the nanostructures before thermal treatment exhibit a well-defined (although not particularly intense) absorption pre-edge peak at ~285 eV that is unequivocally attributed to π-bonded carbon [33], thus indicating that a fraction of sp^2 bonds is indeed present in the as-implanted phase. Contrarily to what is commonly observed in amorphized carbon, this spectral feature does not increase upon thermal annealing, but rather

187 completely disappears, which unequivocally indicates that the sp^2 bonds are absent from the

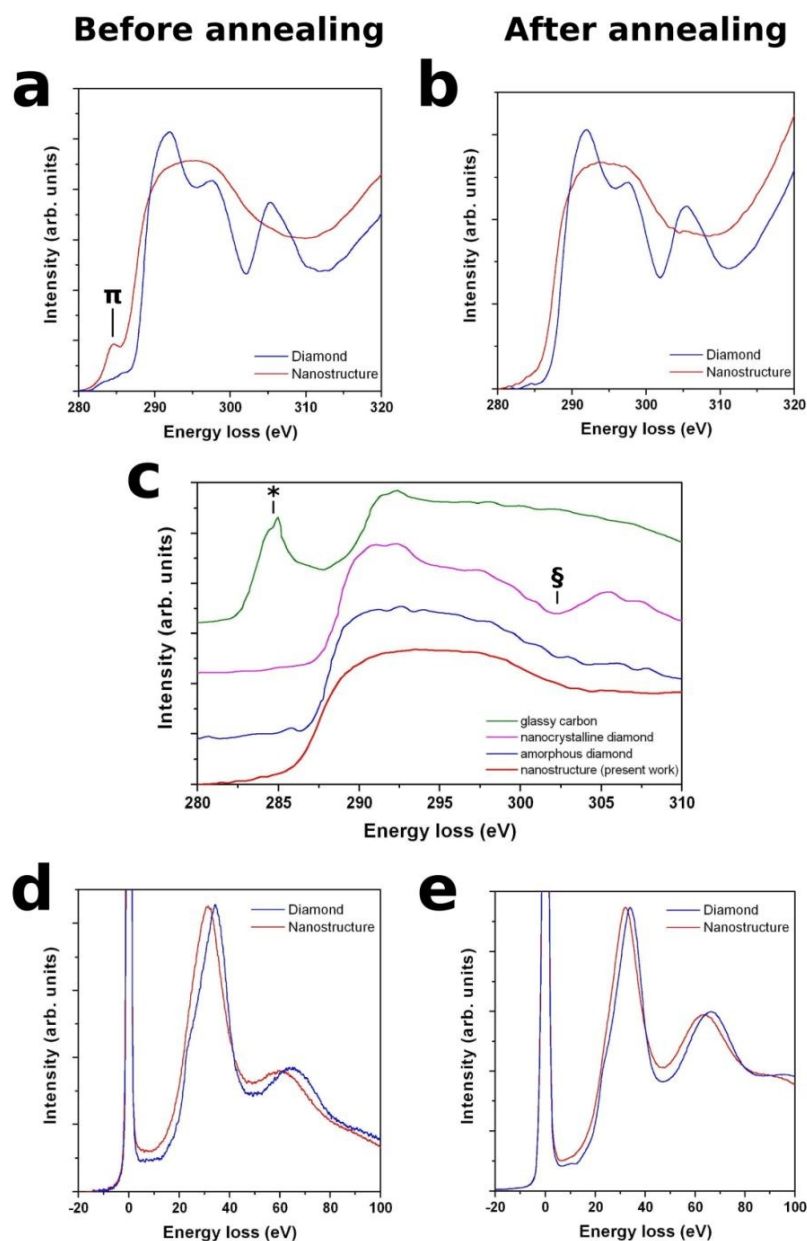188 annealed nanostructure within the detection limit of this very sensitive technique.

189

190 ***Fig. 3*** *Results of cross-sectional EELS spectroscopy of the nanostructures. K-edge absorption features of both*

191 *the nanostructure (red plots) and the surrounding diamond matrix (blue plots) are reported for both the as-*

192 *implanted (**a**) and thermally processed (**b**) sample. The pre-edge peak at ∼285 eV, which is attributed to*

193 *π-bonded carbon, is visible in a, while it is entirely absent in b. **c** Present experimental data are compared to the*

194 *data reported for fully-sp3 bonded amorphous carbon in [20], as well as to the characteristic spectra of glassy*

195 *carbon (in which the ∼285 eV feature is labeled as *) and nanocrystalline diamond (whose characteristic post-*

196 *edge structure is labeled as §). Low-loss spectra exhibit a characteristic downshift in the plasmon-related*

197 *features, both before (**a**) and after (**b**) thermal processing.*

198

199   For the sake of comparison, Fig. 3c reports our experimental data together with the EELS

200   spectrum collected from the fully sp^3-bonded amorphous carbon phase investigated in [20]:

201   the mutual similarity is striking, particularly considering that both spectra entirely lack the

202   features associated with glassy carbon and nanocrystalline diamond (marked as * and § in the

203   respective reference spectra). The EELS features in the low-energy-loss range reported in

204   Figs. 3d and 3e exhibit plasmon peaks which are indicative of the electron densities in the

205   corresponding phases. Both before and after thermal annealing, a systematic shift to lower

206   energy losses of the plasmon peak positions is observed from the nanosctructures with

207   respect to the ~34 eV peak, which is characteristic of the surrounding diamond matrix [14,

208   34, 35, 36]. These shifts can be interpreted on the basis of the lower atomic density of the

209   nanostructures, by adopting the following formula [36-38]:

210

211    $$E_p = \sqrt{\frac{n_e \cdot e^2}{\varepsilon_0 \cdot m^*}}$$

212

213   where E_p is the plasmon energy, m^* and e are the effective mass and charge of electron, ε_0 is

214   the vacuum dielectric constant and n_e is the valence electron density.

215   Given the mass density (i.e. 3.515 g cm^{-3}) and plasmon peak position (i.e. ~34 eV) of the

216   surrounding diamond matrix, and under the assumption that the same electron effective mass

217   can be adopted for the different phases under investigation [38], it is possible to estimate the

218   electron and (and thus mass) density within the nanochannels from the position of the

219   corresponding plasmon peaks. Under these approximations, the (31.0 ± 0.3) eV and

220   (32.6 ± 0.3) eV plasmon peak positions measured from the nanostructures before and after

221   thermal annealing yield mass density estimations of (2.92 ± 0.06) g cm^{-3} and

222   (3.27 ± 0.07) g cm^{-3}, respectively.

223   This result is indicative of the fact that: i) the implantation process results in a substantial

224   density variation within the nanochannels, despite the strong compressive stress exerted by

225   the rigid surrounding diamond matrix; and ii) the disappearing of sp^2 bonds within the

226   nanochannels upon thermal annealing determines a substantial increase of mass density with

227   respect to the as-implanted sample, which closely approaches the density of pristine diamond

228   and is fully compatible with the estimation (i.e. 3.3 g cm^{-3}) provided for the fully sp^3-bonded

229   amorphous carbon phase reported in [20].

230 Finally, we remark that thermal annealing results in radically different structural features

231 across the previously defined "continuous shallow layer" located above the nanochannels

232 (see Fig. 4a). While (as much as observed from the nanochannels) the continuous shallow

233 layer is characterized by TEM diffractometry features that are indicative of a fully

234 amorphized phase (see Fig. 4b), the EELS spectrum (see Fig. 4c) exhibits the strong

235 absorption pre-edge peak at ~285 eV. Such a difference is attributed to the different

236 geometries of the two types of structures, while all other fabrication and processing

237 parameters (irradiation, thermal annealing) are the same. This strongly indicates that the

238 peculiar stress field developed in correspondence of the nanostructures is primarily

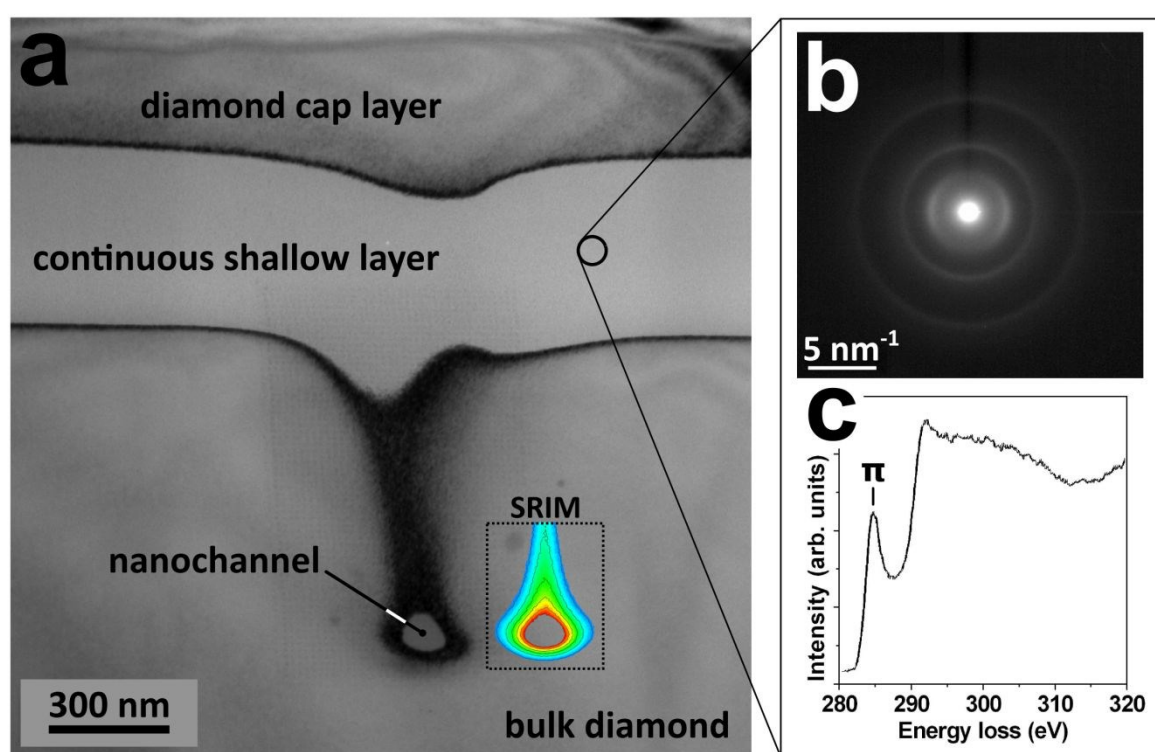239 responsible for the formation of an amorphous full-sp^3 network.

240

241

242 **Fig. 4** *Structural properties of the continuous shallow layer located above the nanostructures, following thermal*

243 *annealing.* **a** *Cross sectional bright-field TEM micrograph from the annealed structure: the labels indicate the*

244 *diamond cap layer, the continuous shallow layer and the nanochannel embedded in the bulk diamond; the inset*

245 *labeled by "SRIM" reports the two-dimensional damage density plot reported in Fig. 1c, for sake of*

246 *comparison.* **b** *TEM diffraction pattern collected from a random region of the continuous shallow layer.* **c**

247 *Corresponding EELS spectrum, clearly exhibiting the strong absorption pre-edge peak at ~285 eV which is*

248 *indicative of a large fraction of sp^2 bonds.*

249

250

251 Our interpretation is confirmed by 2D finite element method (FEM) mechanical analysis. By

252 simulating the constrained expansion undergone by the two implanted regions, it is possible

253 to highlight a significant volumetric stress build up in the 40–50 GPa range (consistently with

254 results in [20]) upon ion implantation.

255 However, as shown in Fig. 5a, the shallow layer (region encircled by the dashed line) does

256 not undergo significant stresses in the vertical (y) direction, while the latter tends to

257 accumulate in the end-of-range region of the nanochannel, due to the confining effect of the

258 surrounding pristine diamond material. The depth variation of σ_y stresses in the nanochannel

259 (Fig. 5b), which reach a peak value of about 48 GPa, while remaining negligible in the

260 shallow layer (shaded area), are identified as the factors that are responsible for the different

261 structures observed in the two regions. Figs. 5c and 5d show the results of analogous

262 numerical simulations carried for the nanostructure after thermal annealing, under the

263 assumption that the latter process results in a conversion to a graphitic phase. In this case, a

264 distribution of relatively high compressive stresses (in the GPa range) still persists. It is worth

265 remarking that stress fields of this order of magnitude are indeed observed in graphitized

266 microstructures created with this technique, such as the ones reported in [22]. The

267 experimental observation that thermal annealing does not result in the graphitization of the

268 nanostructure is therefore attributed to the fact that the strong stress fields established around

269 the nanostructure upon ion implantation are instead fully relaxed (i.e. residual stresses in the

270 Pa range) upon the formation of a fully sp^3-bonded amorphous carbon phase, as confirmed by

271 the simulations reported in Figs. 5e and 5f. In our interpretation, the stress state responsible

272 for the transition to sp^3 bonds is established before the thermal annealing. The initially

273 strongly stressed nanochannels therefore transition to a fully sp^3-bonded amorphous phase

274 upon thermal annealing, and only subsequently are the stresses relaxed.

275 As mentioned above, an experimental assessment of the local stresses established across

276 amorphized/graphitized structures embedded in the diamond matrix is in general possible by

277 means of confocal micro-Raman spectroscopy, both before and after thermal annealing, as

278 already demonstrated for micrometer-sized regions [22]. This was not possible (either by

279 conventional or tip-enhanced Raman spectroscopy) in the case of the nanostructures reported

280 in the present work, due to (respectively) limited spatial resolution and spectral sensitivity of

281 the available techniques. Nonetheless, it is worth remarking that EELS provided direct

282 experimental insight into the local mass density of the nanostructures, which directly

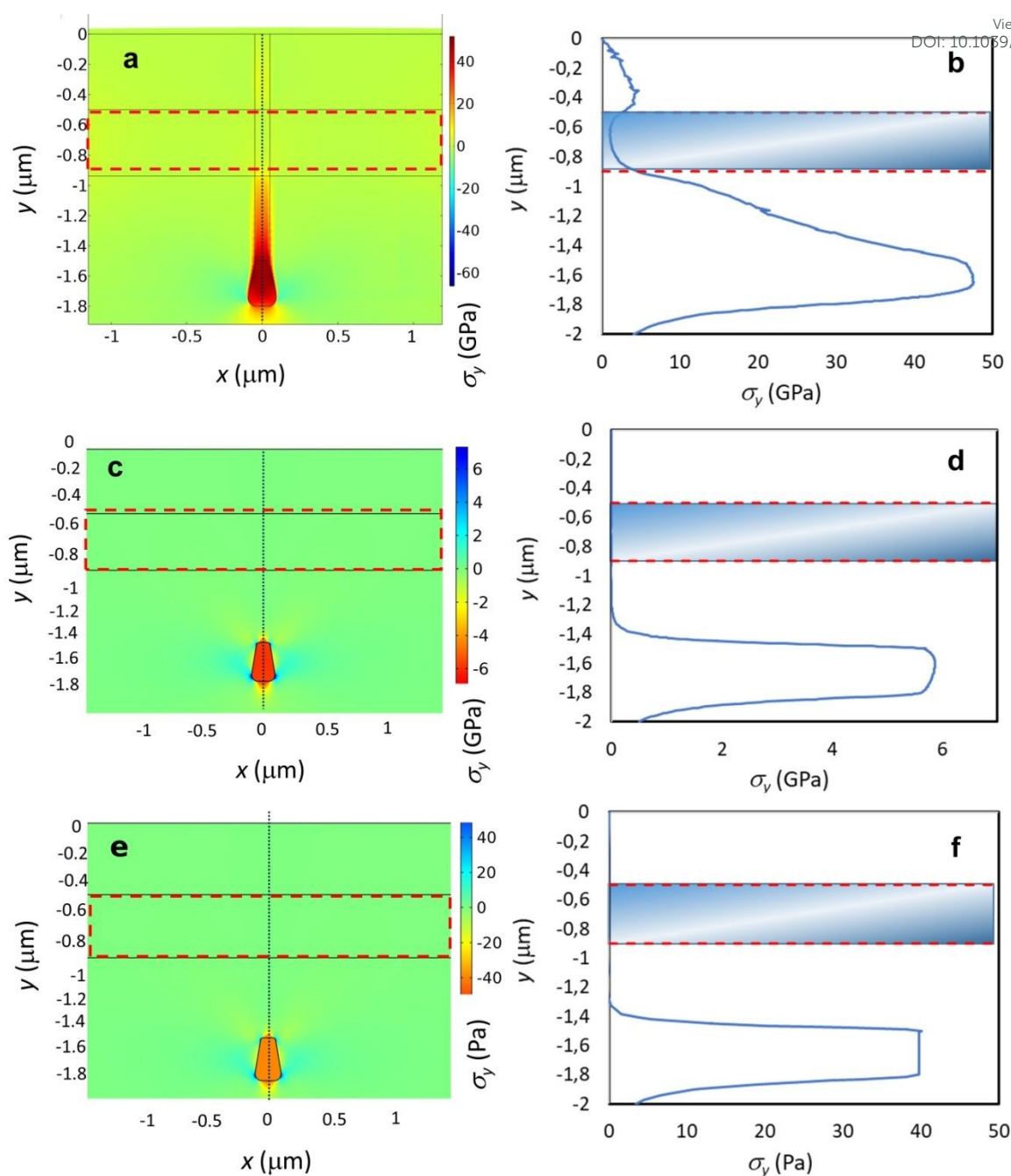283 translated into the above-described numerical simulations.

284

Fig. 5 *Results of FEM simulations of stress distributions across the structures.* **a** *Map of the principal stress in the vertical direction (σ_y) in a cross section of the as-implanted diamond: stresses develop in the nanochannel, and are negligible in the shallow layer (dashed line).* **b** *σ_y variation along the dotted line in* **a***; the shaded region indicates the shallow layer location.* **c, d** *Results of analogous simulations carried for the nanostructure after thermal annealing, under the assumption that this process results in a conversion to a graphitic phase: residual stresses in the GPa range are still persistent.* **e, f** *Results of analogous simulations carried for the nanostructure after thermal annealing, under the assumption that the latter process results in a conversion to a fully sp^3-bonded amorphous carbon phase: very small residual stresses in the 10 Pa range are obtained in this case.*

293

294   ## 3. Conclusions

295   In conclusion, the reported results indicate the possibility of creating an amorphous carbon

296   phase entirely based on sp^3 chemical bonds, by means of ion-induced structural damage in

297   nanometer-sized regions embedded within the bulk diamond structure, followed by thermal

298   annealing. As confirmed by numerical simulations, the strong three-dimensional mechanical

299   stress state developed within the nanostructures is the required condition for the formation of

300   this peculiar carbon phase without the need of applying external pressure during the

301   annealing process: the key role played in the formation of this phase by internal stress fields

302   surrounding the nanostructures is demonstrated by the fact that control structures with

303   different geometries, and hence stress states, produce a radically different amorphous phase

304   containing a substantial fraction of sp^2 bonds. It is worth remarking that, although playing an

305   essential role, the high mechanical stresses established across the nanostructures are not

306   sufficient for the formation of the reported fully sp^3-bonded amorphous phase. As reported in

307   Fig. 3a, a fraction of sp^2-bonded carbon is indeed persistent in the strongly stressed

308   nanostructures formed upon ion implantation, and it is converted only upon the subsequent

309   thermal annealing. The necessity of carefully controlling both pressure and temperature

310   parameters for the formation of the reported carbon phase is qualitatively consistent with

311   what is reported in previous works [17-19] and particularly in Ref. [20]. Furthermore, it is

312   coherent with our current understanding of the complex pressure temperature landscape

313   around the triple point in the phase diagram of carbon [23]. We envisage that an accurate

314   numerical simulation of this carbon-based system in the reported range of

315   pressure/temperature parameters would shed significant insight into the mechanisms leading

316   to the formation of the fully sp^3-bonded amorphous carbon phase.

317   The results presented in this work shed useful insight into the mechanisms leading to the

318   formation of fully-sp^3-based amorphous phases in carbon, and display appealing applications

319   in fields where high-pressure carbonaceous phases could be implemented in integrated

320   devices, such as for example room-temperature superconducting devices [39].

321   Besides the fundamental relevance of this finding in the understanding of the formation of

322   exotic carbon phases, the use of focused/collimated ion beams enables the direct fabrication

323   of such nanostructures in complex patterns and arrangements, with appealing perspectives in

324   nanomechanical systems and integrated nano-optics.

325

326

4. Methods

4.1 Samples

The experiments were performed with equivalent results on different types of commercially-available artificial single-crystal diamond samples, namely a $3\times3\times0.5$ mm^3 sample produced by Element Six^{TM} with the Chemical Vapor Deposition technique, and a $3\times3\times1.5$ mm^3 sample produced by Sumitomo Electrics^{TM} with the High pressure High Temperature synthesis technique. The former sample is classified as a type IIa "optical grade" crystal, with substitutional nitrogen and boron concentrations lower than 1 ppm and 0.05 ppm, respectively. The latter sample is classified as a type Ib crystal, with substitutional nitrogen concentration comprised between 10 ppm and 100 ppm. In both cases, the samples are cut along the 100 crystal direction and are optically polished on the two opposite large faces. After accurate surface cleaning, a ~1.3 μm thick Cu layer was deposited by thermal evaporation in high vacuum conditions. Conventional FIB micromachining with a 30 keV Ga$^+$ ion beam was used for the mask fabrication. A Quanta 3D FEG DualBeam^{TM} apparatus equipped with Nanometer Pattern Generation System (from J. C. Nabity) was used for the patterning of linear nano-apertures of 100 nm width. A protective thin layer (~100 nm) of the mask was left in correspondence of each aperture, in order to avoid the superficial damage induced by Ga$^+$ ions. After the FIB mask definition, the sample was irradiated with a beam of 1 MeV He$^+$ ions at the 0° beam line of the AN2000 accelerator of the INFN National Laboratories of Legnaro. Ion current density was ~500 nA mm^{-2} and the irradiation fluence was 5×10^{16} cm^{-2}.

4.2 Samples characterization

Sample characterization was performed at the Microscopy laboratories of the Bio21 Institute (University of Melbourne). 150-nm-thick cross-sectional lamellae were cut in the {110} crystallographic direction by conventional FIB micromachining employing 30 keV Ga$^+$ ions. In order to reduce FIB-induced damage layers, the lamellae were finally cut with a 5 keV Ga$^+$ beam from the same FIB facility. High-resolution transmission electron microscopy (HRTEM) were performed with a Tecnai TF20 electron microscope (S-TWIN objective lens, 0.24 nm point resolution) transmission electron microscope operated at 200 keV. Selected area diffraction patterns (SADP) were collected with smallest aperture (~180 nm effective diameter in specimen plane). Electron energy loss spectroscopy (EELS) measurements and

360 spectrum imaging were conducted in STEM mode, with 1 nm probe beam diameter, 2.2 mrad

361 convergence semi-angle and 16 mrad collection semi-angle at 200 kV (FEI Tecnai TF30)

362 using Gatan GIF Quantum™ 965 energy filter with dual EELS capability. All TEM and

363 EELS data processing was carried out using Gatan Digital Micrograph (DM) software.

364

365 **4.3 Numerical simulations**

366 The MeV ion induced structural damage profiles were numerically modeled by means of the

367 SRIM Monte Carlo Code (2013.00 version) [27]. All simulations were performed in the

368 "Detailed calculation with full damage cascades" mode, by setting a displacement energy

369 value of 50 eV for diamond [40, 41]. The beam was assumed to be impinging on the surface

370 at normal incidence with the mask perfectly aligned to the ion beam. A large (i.e. >100'000)

371 number of ion trajectories was simulated. The SRIM output yields profiles of linear damage

372 density, parameterized as number of vacancies per unit length in the depth direction.

373 Volumetric vacancy densities were estimated from the above-said linear density profiles and

374 the implantation fluences, by modeling the cumulative effect of implanted ions within a

375 simple linear approximation, which does not take into account complex processes such as

376 self-annealing, ballistic annealing and defect interaction.

377 To gain further insight in the process of amorphization and estimate the stresses acting on the

378 irradiated region, 2-D FEM simulations were performed using Comsol Multiphysics.

379 Consistently with the results of cross-sectional TEM microcopy (see Fig. 4a), a 5×5 μm^2

380 diamond cross section was considered, in which a 0.1×1.8 μm^2 implanted diamond strip is

381 incorporated, representing the nanochannel, including a terminal trapezoidal region to

382 account for straggling effects, and a 5×0.5 μm^2 strip representing the shallow layer (see

383 Fig. 5). For the as-implanted sample, material parameters are: diamond density

384 $\rho_d = 3.52$ g cm^{-3}, amorphous carbon density $\rho_{aC} = 2.06$ g cm^{-3}, diamond Young's modulus

385 $E_d = 1220$ GPa, amorphous carbon Young's modulus $E_{aC} = 21.38$ GPa, [42, 43]. The density

386 of the implanted region before annealing was calculated as a function of the induced damage

387 density as reported in [44], i.e.:

388

389
$$\rho(y) = \rho_d - (\rho_d - \rho_{aC}) \cdot \Phi(y)$$

390
$$\Phi(y) = 1 - exp\left[-\frac{F \cdot \lambda(y)}{\gamma\left(1 - \rho_{aC}/\rho_d\right)}\right]$$

391 where $\gamma = 1.77 \times 10^{23}$ cm^{-3} is the atomic density of diamond, F is implantation fluence and $\lambda(y)$

392 is the linear vacancy density, as derived from SRIM code. The equation accounts for defect

393 recombination and damage saturation effects occurring in the crystal [45].

394 The Young's modulus decrease as a function of the vacancy density can be expressed as:

395
$$E(y) = E_d - (E_d - E_{aC}) \cdot \Phi(y)$$

396 The density decrease due to irradiation generates a constrained expansion of the implanted

397 volume, i.e. residual strains in the $i = x,y$ directions that can be expressed as follows:

398
$$\varepsilon_i(y) = \sqrt[3]{\frac{\rho_d}{\rho(y)}} - 1$$

399 In the case of the sample after thermal annealing, the simulations were carried under two

400 alternative hypotheses, i.e. a conversion of the nanostructure to a graphitic phase (see Figs. 5c

401 and 5d) or to a fully sp^3-bonded amorphous carbon phase (see Figs. 5e and 5f). In the former

402 case, the following structural parameters were adopted: $\rho_g = 2.1$ g cm^3, Young's modulus

403 $E_g = 21$ GPa. In the latter case, the following structural parameters were adopted:

404 $\rho_{a-d} = 3.3$ g cm^3 [20, this work], $E_{a-d} = 1123$ GPa [20].

405

Authors contributions

407 F.P. conceived this study and coordinated the experimental campaign. A.B. and F. S. M.

408 prepared the samples (masking and post-irradiation processing). V. R. and F. P. prepared the

409 samples (ion irradiation). F. B. developed the numerical model of the internal stresses. P. O.

410 contributed to data analysis and compiled the manuscript (with contributions from all co-

411 authors). S. R. performed TEM and EELS characterization.

412

Conflicts of interest

414 There are no conflicts to declare.

415

Acknowledgments

Nanoscale Advances Accepted Manuscript

References

[1] B. Sundqvist, Carbon under pressure. Phys. Rep. 1-73, 909.

[2] Yang, N. (guest ed.) *Novel Aspects of Diamond - From Growth to Applications* (Springer, 2019).

[3] Jackman, R. B. et al. (guest ed.) Special issue on diamond electronics. *Semicond. Sci. Technol.* **18**, S1-S140 (2003).

[4] Acosta, V. et al. (guest ed.) Nitrogen-vacancy centers: Physics and applications. *MRS Bull.* **38**, 127-167 (2014).

[5] Nemanich, R. J. et al. (guest ed.) CVD diamond - Research, applications, and challenges. *MRS Bull.* **39**, 490-548 (2014).

[6] Demazeau, G. A century of high pressure: technological and scientific developments. *C. R. Chim.* **12 (9)**, 933-942 (2009)

[7] Varnin, V. P. et al. The state of the art in the growth of diamond crystals and films. *Inorg. Mater.* **42**, S1-S18 (2006).

[8] Hess, P. The mechanical properties of various chemical vapor deposition diamond structures compared to the ideal single crystal. *J. Appl. Phys.* **111 (5)**, 051101 (2012).

[9] Li, G. et al. The manufacturing and the application of polycrystalline diamond tools - A comprehensive review. *J. Manuf. Sci. Eng.* **56 (A)**, 400-416 (2020).

[10] Gruen, D. M. Nanocrystalline diamond films. *Annu. Rev. Mater. Sci.* **29**, 211-259 (1999)

[11] Huang, Q. et al. Nanotwinned diamond with unprecedented hardness and stability. *Nature* **510**, 250-253 (2014).

[12] Al Mahmud, K. A. H. An updated overview of diamond-like carbon coating in tribology. *Crit. Rev. Solid State* **40 (2)**, 90-118 (2015).

[13] Tyagi, A. A critical review of diamond like carbon coating for wear resistance applications. *Int. J. Refract. Hard. Met.* **78**, 107-122 (2019).

[14] LiBassi, A. et al. Density, sp3 content and internal layering of DLC films by X-ray reflectivity and electron energy loss spectroscopy. *Diam. Relat. Mater.* **9**, 771-776 (2000).

[15] Robertson, J. Diamond-like amorphous carbon. *Mater. Sci. Eng. R: Rep.* **37**, 129-281 (2002).

[16] McKenzie, D. R. et al. Compressive-stress-induced formation of thin-film tetrahedral amorphous carbon. *Phys. Rev. Lett.* **67**, 773–776 (1991).

[17] Lin, Y. et al. Amorphous diamond: a high-pressure superhard carbon allotrope. *Phys. Rev. Lett.* **107**, 175504 (2011).

479   [18] Goncharov, A. F. Graphite at high pressure: pseudomelting at 44 GPa. *Zh. Eksp. Teor.*

480   *Fiz.* **98**, 1824–1827 (1990).

481   [19] Yao, M. et al. Transparent, superhard amorphous carbon phase from compressing glassy

482   carbon. *Appl. Phys. Lett.* **104**, 021916 (2014).

483   [20] Zeng, Z. et al. Synthesis of quenchable amorphous diamond. *Nat. Comm.* **8**, 322 (2017).

484   [21] Prawer, S. et al. Investigation of carbon near the graphite-diamond-liquid triple point.

485   *Phys. Rev. Lett.* **69 (20)**, 2991-2994 (1992).

486   [22] Olivero, P. et al. Splitting of photoluminescent emission from nitrogen–vacancy centers

487   in diamond induced by ion-damage-induced stress. *New J. Phys.* **15**, 043027 (2013).

488   [23] Hunn, J. D. et al. Raman Scattering from MeV-ion implanted diamond. *Phys. Rev. B* **52**

489   **(11)**, 8106 (1995).

490   [24] Cagliero, S. et al. Insight into non-linearly shaped superconducting whiskers via a

491   synchrotron nanoprobe. *Supercond. Sci. Technol.* **25 (12)**, 125002 (2021).

492   [25] Torsello, D. et al. Monte Carlo analysis of the oxygen knock-on effects induced by

493   synchrotron x-ray radiation in the $Bi_2Sr_2CaCu_2O_{8+\delta}$ delta superconductor. *Phys. Rev. Mater.* **2**

494   **(1),** 14801 (2018).

495   [26] Mino, L. et al. Maskless x-ray writing of electrical devices on a superconducting oxide

496   with nanometer resolution and online process monitoring. *Sci Rep.* **7**, 9066 (2017).

497   [27] Ziegler, J. F. et al. *2008 SRIM—The Stopping and Range of Ions in Matter* (Mormsville,

498   NC: Ion Implantation Press)

499   [28] Gippius, A. A. et al. Formation and characterization of graphitized layers in ion-

500   implanted diamond. *Diamond Relat. Mater.* **8**, 1631-1634 (1999).

501   [29] Hickey, D. P. et al. Amorphization and graphitization of single-crystal diamond - A

502   trasmission electron miscroscopy study. *Diamond Relat. Mater.* **18**, 1353-1359 (2009).

503   [30] Rubanov, S. et al. Ion implantation in diamond using 30 keV Ga^+ focused ion beam.

504   *Diamond Relat. Mater.* **20**, 1160-1164 (2011).

505   [31] Drumm, V. S. et al. Surface damage on diamond membranes fabricated by ion

506   implantation and lift-off. *Appl. Phys. Lett.* **98**, 231904 (2011).

507   [32] Motochi, I. et al. Surface Brillouin scattering on annealed ion-implanted CVD diamond.

508   *Diamond Relat. Mater.* **56**, 6-12 (2015).

509   [33] Muller, D. A. et al. Mapping sp2 and sp3 states of carbon at sub-nanometre spatial

510   resolution. *Nature* **366**, 725-727 (1993).

511   [34] Bursill, L. A. et al. Plasmon response and structure of nanocrystalline diamond powder.

512   *Philos. Mag. A* **76 (4)**, 769-781 (1997).

513 [35] Sato, Y. et al. High energy-resolution electron energy-loss spectroscopy analysis of

514 dielectric property and electronic structure of hexagonal diamond. *Diamond Relat. Mater.* **25**,

515 40-44 (2012).

516 [36] Cuomo, J. J. et al. Sputter deposition of dense diamond-like carbon films at low

517 temperature. *Appl. Phys. Lett.* **58 (5)**, 466-468 (1991).

518 [37] Fallon, P. J. et al. Properties of filtered-ion-beam-deposited diamondlike carbon as a

519 function of ion energy. *Phys. Rev. B* **48 (7)**, 4777-4782 (1993).

520 [38] Ferrari, A. C. et al. Density, sp^3 fraction, and cross-sectional structure of amorphous

521 carbon films determined by x-ray reflectivity and electron energy-loss spectroscopy. *Phys.*

522 *Rev. B* **62 (16)**, 11089-11103 (2000).

523 [39] Snider, E. et al. Room-temperature superconductivity in a carbonaceous sulfur hydride.

524 *Nature* **586**, 373-377 (2020).

525 [40] Wu, W. et al. Molecular-dynamics study of single-atom radiation damage in diamond.

526 *Phys. Rev. B* **49 (5)**, 3030-3035 (1994).

527 [41] Saada, D. et al. Transformation of diamond (sp^3) to graphite (sp^2) bonds by ion impact.

528 *Int. J. Mod. Phys. C* **9 (1)**, 61-69 (1998).

529 [42] Wei, Y. X. et al. Soft phonons and phase transition in amorphous carbon. *Phys. Rev. B*

530 **72**, 012203 (2005)

531 [43] Fairchild, B. A. et al. Mechanism for the Amorphisation of Diamond. *Adv. Mater.* **24**,

532 2024-2029 (2012).

533 [44] Battiato, A. et al. Softening the ultra-stiff: Controlled variation of Young's modulus in

534 single-crystal diamond by ion implantation. *Acta Mater.* **116**, 95-103 (2016).

535 [45] Bosia, F. et al. Direct measurement and modelling of internal strains in ion-implanted

536 diamond. *J. Phys. Condens. Matter* **25 (38)**, 385403 (2013).